The gravitationally lensed blazar PKS 1830−211 seen by ALMA

Determination of the time delay between the lensed images

Master's thesis in Applied Physics

MARIANA DAVID

Department of Earth and Space Sciences
CHALMERS UNIVERSITY OF TECHNOLOGY
Gothenburg, Sweden 2016

Master's thesis in Applied Physics

The gravitationally lensed blazar PKS 1830−211 seen by ALMA

Determination of the time delay between the lensed images

Mariana David

Department of Earth and Space Sciences
Radio Astronomy and Astrophysics Group
Chalmers University of Technology
Gothenburg, Sweden 2016

The gravitationally lensed blazar PKS 1830−211 seen by ALMA:
Determination of the time delay between the lensed images
MARIANA DAVID

Supervisors: Sébastien Muller and Ivan Martí-Vidal, Department of of Earth and Space Sciences
Examiner: Cathy Horellou, Department of of Earth and Space Sciences

Department of of Earth and Space Sciences
Radio Astronomy and Astrophysics Group
Chalmers University of Technology
SE-412 96 Gothenburg
Telephone +46 31 772 1000

Cover: The majestic Milky Way descends over ALMA. Credit: ALMA (ESO/NAOJ/NRAO), C. Padilla

Typeset in LaTeX
Printed by Chalmers Reproservice
Gothenburg, Sweden 2016

The gravitationally lensed blazar PKS 1830−211 seen by ALMA:
Determination of time delay between lensed source
MARIANA DAVID
Department of Earth and Space Sciences
Chalmers University of Technology

Abstract

PKS 1830−211 is a blazar lensed by a foreground galaxy. The alignment of these two objects causes the formation of two distinct compact images embedded in a pseudo-Einstein ring. In this master thesis, we use multi-epoch and multi-frequency data, collected by the Atacama Large Millimeter/submillimeter Array (ALMA) in 2012 and 2014, with the aim of determining the time delay between the two lensed images. These have been resolved in all observations and, by modelling the flux of the North-East image and the flux ratio of both images, the time delay was found to be (28 ± 3) days. This result can be used in future work to better constrain the lens model of the system constituted by the blazar and its foreground galaxy. Furthermore, the physics of the jet was studied by interpretation of the measurements and spectral indices which varied between both periods and were found to be (0.77 ± 0.03) and (0.35 ± 0.10) in 2012 and 2014 respectively.

Keywords: blazar – PKS 1830−211, gravitational lensing, interferometry, data modelling.

Acknowledgements

Opportunities came at different times and in various forms. They can be a position you accept, a course you pick, a study trip you go to, a meeting you ask for. And once the opportunity is presented, there is the choice of taking it or wait for the next one. During the last year, I have encountered many opportunities which have challenged my discipline, intellect and values. For that, there are many people whom I am very grateful to.

In Onsala, I want to show my deepest appreciation for my supervisors, Sébastien and Ivan, for their time, patience, encouragement, knowledge, guidance and perseverance. I hope that in some years from now my eyes will be as alive and excited at work as frequently I saw yours. Thank you Cathy for warmly welcoming an inexperienced student whose only certain was to write her Master's thesis in Astronomy and for sharing your experience and advices with her. I also want to thank the other employees, PhD students and researchers for Wednesday's seminars, lunch discussions and casual walks. It was an enriching experience to be submersed in your world.

Outside Onsala, there are many people responsible for the busiest period in my life. Thank you members of BEST, specially Anusha, my rock. Thank you Rickard, Maria, Poornima, Carolina, Marina, Rathi, Teja and Andreas for your constant availability and support. Thank you Laura for sharing the occasional pains of being a student.

Finally, thank all my family (everyone!) for the video-calls, mailed packages and nice vacations. Mãe, pai, Luís e Afonso, obrigada por me darem a liberdade de caminhar ao meu ritmo e me incentivarem a procurar novas experiências.

Mariana David
Gothenburg, March 2016

"You have to trust that the dots will somehow connect in your future."
Steve Jobs

Contents

List of Figures

List of Tables

1

Introduction

In this chapter the concepts of gravitational lensing, quasars, blazars and radio astronomy are presented, followed by the introduction to the blazar PKS 1830−211 and its lensing galaxy.

1.1 Gravitational lensing

After the theory of general relativity, the notion that light always follows a straight path was abandoned. As a matter of fact, light bends when propagating near very massive objects. And the more massive an object is or the closer from it the light propagates, the more curved the light's path gets. The theory of general relativity also explains that this happens because the spacetime around very massive objects gets distorted and light follows its curvature as long as it is the shortest propagation path. This effect only gets strong enough to be measured on large scales, equivalent to the masses of neutron stars, black holes and clusters of galaxies. And indeed it has been observed.

In 1979, two quasars with incredibly similar magnitudes, spectra and redshifts were discovered very close to each other [16]. In fact, their properties were too similar to come from different sources and later were found to be two images from the same quasar, Q 0957+561, originated due to *gravitational lensing*.

The principle of gravitational lensing is sketched in Figure 1.1. An observer at point **O** looking at a certain direction only sees the massive object **M** that conceals the bright source **S** located at the same line of sight. However, due to the strong gravity of **M**, the radiation emitted by **S** bends and changes its trajectory, reaching **O**.

Since each trajectory of light corresponds to an image of the source **S'**, the observer sees a ring, the *Einstein ring*, only when **M** is perfectly symmetric on the line of sight. The time needed for the light to cross the paths **A** and **B** is the same. On the other hand, if **M** is not perfectly centred at the line of sight, light goes through different paths relatively to **M** and instead a broken pseudo-ring is seen, as well as different components. Moreover, a time delay between the light-rays going through the paths **A** and **B** is now measurable and one of the light curves becomes the leading image. It should also be noted that each light curve shows its own magnification that is perceptible by **O**. Since gravitational lensing is an achromatic process, which means that it does not depend on the emission frequency, and assuming that all frequencies are emitted from the same region in the source, the time delay between core images is independent of the measured frequency. Therefore, measuring and comparing the time delays at different frequencies can enlighten about the energetic mechanisms happening at different regions of the source.

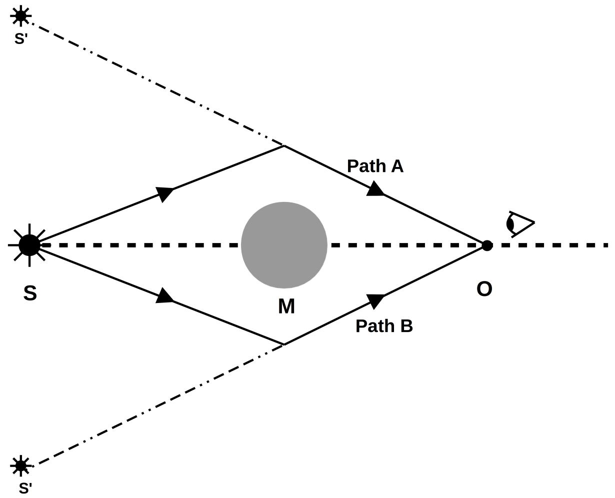

Figure 1.1: Illustration of gravitational lensing. The source **S** emits radiation that is bent due to the gravitational field of a very massive object **M**. An observer at **O** does not see the real source, but rather an image **S'** that depends on the path taken by the radiation.

1.1.1 Calculation of Hubble constant from time delay

The Hubble constant is one of the most important quantities in Astronomy as it is directly related to the age, size and expansion rate of Universe. Moreover it is also used to easily calculate distances of cosmological objects according to the expression

$$v = H_0 r \tag{1.1}$$

where v is the recessional velocity (at which the object is moving away from Earth), H_0 the Hubble constant and r the distance from Earth [16].

A way to determine this constant is by measuring a galaxy's redshift, its distance from Earth and applying the equation 1.1. This can be difficult since it requires a reference bright source with special characteristic, called "standard candle". But there are other methods that require the time delay of the lensed images.

In 1964, a new approach that used the time delay between lensed images as a scaling factor was implemented. In case there are two similar universes, being one larger than the other as in Figure 1.2, measuring the angular separation between the lensed images, their relative positions to the lensing galaxy and their magnification ratio results in the exact same values. Hence a scaling factor is needed in order to distinguish both situations [16]. Since the time delay between lensed images does depend on the size of the respective universe, it can be used as scaling factor and the Hubble constant determined with the equation

$$H_0 = K \frac{(\Delta\theta)^2}{\Delta\tau} \tag{1.2}$$

where K is a constant that depends on the mass distributions of the lens, $\Delta\theta$ is the angular separation between lensed images and $\Delta\tau$ the time delay [17, 18].

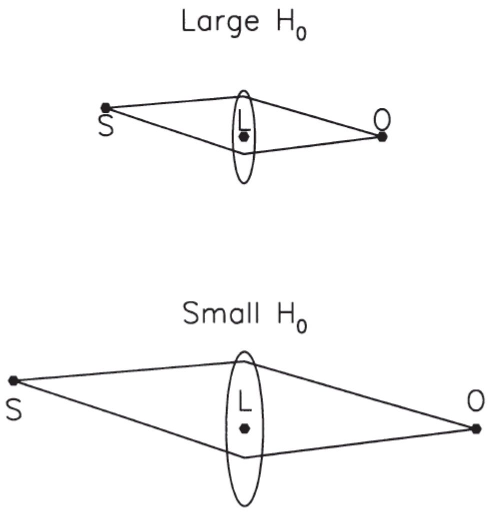

Figure 1.2: In two similar universes, one of them bigger than the other, the observation of the gravitational lens properties (angular separation between lensed images, their relative positions to the lensing galaxy and their magnification ratio) would result in the same values. Therefore a scaling factor such as the time delay between lensed images is necessary in order to distinguish both situations. Image from [16].

1.2 Quasars and blazars

In 1963, a strong radio source similar to stars was observed and named *Quasistellar Radio Source* which means "star-like radio source". This was the quasar 3C 273 and was identified during a lunar occultation. Quasars are very massive compact objects, so bright that can outshine their host galaxies. With the energy output equivalent to the brightness of billions stars (around 10^{39} W [3]) coming from one single object, they are the most powerful element of the active galactic nuclei family, which differ from normal galaxies due to the existence of a a very massive and compact object in their nucleus, a supermassive black hole in an active phase, that will be discussed further on.

Quasars have been detected at different redshifts, ranging from $z = 0.16$ to $z = 6$, which corresponds to cosmological distances between 770 and 59,000 Mpc. (For comparison, the closest galaxy from the Milky Way, Andromeda, is located at 778 kpc.) Furthermore, the time scale of their brightness variability can be of the order of days or less, which multiplied by the speed of light, implies dimensions of the emitting region not much larger than the solar system.

The Unifying Model takes *blazars* to be a particular geometric configuration of quasars, when observed face-on so that the highly collimated outflow that they exhibit is emitted in the line of sight of the observer.

Structure modelling

The Figure 1.3 shows a radio image of the quasar 3C175, obtained with the Very-Large Array (VLA). Its structure can be describe in the following: the small bright point at the centre of the picture can be explained by an accretion disk surrounding a supermassive black hole. Together they emit two highly collimated jets of plasma which then disrupt into two opposite lobes. Especially brighter zones are seen in the lobes, called hotspots. It should be mentioned that the reason why only one jet is seen in the Figure 1.3 is because the velocity of the visible jet had a component propagating towards Earth, so that its luminosity was boosted relatively to its counterpart due to relativistic effects [7]. Detectors would need greater sensitivity in order to detect the second jet, or counter jet.

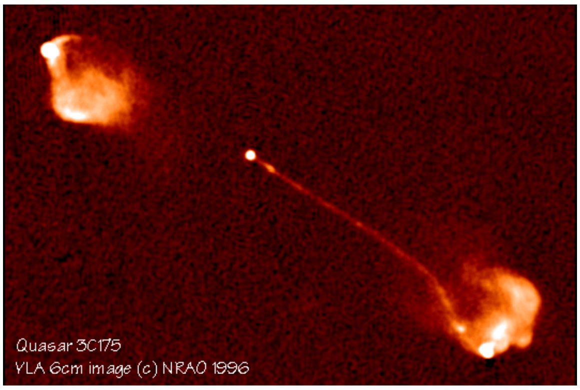

Figure 1.3: VLA image of the quasar 3C175. The most plausible model that describes this structure is the existence of a central supermassive black hole surrounded by a bright accretion disk, from which jets are emitted that feed the double radio lobes. Here prominent hotspots are visible. Only one jet is visible due to relativistic effects. (Credit: NRAO/AUI/NSF. Investigators: Alan Bridl, David Hough, Colin Lonsdale, Jack Burns, and Robert Laing) [8]

Blazars present jets of highly polarized synchrotron emission, that can only be produced when relativistic charged particles are accelerated in spiral trajectories around magnetic field lines. The magnitude of blazars' strong magnetic fields involved is believed to be of the order of $10^3 - 10^4$ Gauss possibly generated by a spinning **supermassive black hole** and accretion disk [9, 10, 11]. A black hole is an object so massive and compact that not even light can escape within a certain radius from its nucleus due to the strong gravitational field. This limit, the Schwarzschild radius, is given by the equation

$$R_{Sch} = \frac{2GM}{c^2} \tag{1.3}$$

This corresponds to compress our Sun from its radius of 696,000 km to mere 3 km. The characteristics of the supermassive black hole have direct effect on the quasar's properties. For example, it has been established a connection between the black holes' mass, spin and mass accretion rate and the fact that only 10% of the quasars' population are radio loud (with radio emission) [10]. However the exact mechanisms involved are still unknown.

Orbiting around the supermasssive black hole there is a flat disk of ionized matter, the **accretion disk**. As it is also very dense, the friction between the plasma particles releases most of the energy that characterises quasars' continuum spectrum, which ranges from radio to X-rays emission. And when particles loose their energy, they slow down and start falling onto the black hole. Then it is believed that a fraction of them is re-emitted as relativistic jets [9, 10, 11].

These relativistic **jets** are highly directional outflows of energy that due to their long lifetime can extend to distances up to 1 Mpc from their source. They are produced by the emission of the equivalent to 1.5 solar masses [12] and collimated by the existing strong magnetic field, together with gradient pressures from the intergalactic medium [9]. Different regions can be identified during the formation of jets. There is a nozzle that boosts the velocity of plasma to relativistic speeds, which is followed by the collimation region and then the conical shape region where the jet propagates freely [7]. The jet power is believed to be correlated with the rotation speed of the accretion disk.

Jets may break down after a certain distance from the core of the black hole, forming two **lobes**, that also present strong emission. Some explanations for this disruption assume a high-density spot in the interstellar medium, natural collapse explained by magnetohydrodynamics, or even some phenomenon related with dark matter [7].

There are many theories for the formation of these powerful objects. The classical one suggests that quasars grew from black hole seeds through continuous accretion after the collapse of primordial stars [13]. However, SMBHs seem to have grown too fast to agree with this explanation and other hypothesis arose, such as primordial galaxies (protogalaxies) merging with each other on a massive nuclear disk [14] or direct accretion of matter at each protogalaxies nucleus due to dynamical instabilities [15].

Nowadays, quasars are widely studied in diverse fields, such as galaxies evolution, cosmology and jet physics.

1.3 Radio astronomy

In radio astronomy the radio emission of astronomical objects is studied, from cm to mm wavelength. It is in this range that some phenomenon become easily detectable. Some examples in the category of thermal processes are the dust blackbody emission, atomic and molecular transitions, whereas some non-thermal radio-emitting processes are masers, synchrotron and free-free emission. As the Earth's atmosphere is relatively transparent to radio wavelengths, radio astronomy can be performed with ground-based observatories, which are less expensive than the optical ones since the surface accuracy is not as demanding. Other advantages of studying radio spectra is that the absorption and scattering of the radiation by the dusty interstellar medium (ISM) becomes negligible [1].

1.3.1 Radio telescopes

A standard radio telescope, or antenna, is composed by a reflector, feed, transmission line and receiver, visible in Figure 1.4. The reflectors are normally parabolic-shaped, and besides providing directionality, they also collect radiation and reflect it to a central focus, at the feed. Here, the astronomical signal is detected when the radio waves interact with conductive material, which is then transmitted, filtered and amplified by the radio receiver. In this way the radio source can be distinguished from the electronic noise and radio background. For optimised observational conditions, radio observatories can be built at high altitudes, where radio noise from civilisation is reduced and the weather is usually dry and cloudless, minimizing the absorption of submillimetre radiation, as well as air turbulence.

Telescopes are characterised by their angular resolution, which is limited by the diffraction of electromagnetic waves. The resolution is dependent on the size of the telescope's aperture, that determines the amount of radiation reaching the detector, and the measured wavelength according to the equation

$$\theta \approx 1.22 \cdot \lambda/d \ , \tag{1.4}$$

where d is the aperture diameter, λ the detected wavelength and θ the telescope's resolution [2]. An application of this equation can be given by comparing radio and optical telescopes. As radio wavelengths are much longer than visible wavelengths (which go from 400 to 700 nm), when aiming, for instance, at a resolution of 1 arcsecond, a radio telescope diameter must be 25 km (considering λ = 10 cm), whereas an optical telescope is required to be 15 cm diameter in order to achieve the same angular resolution (for λ = 600 nm).

As the resolution of a single radio antenna is limited to its diameter, techniques to improve spacial resolution by combining several radio antennas in multiple-element array have been developed.

Figure 1.4: ALMA antennas at Chajnantor. Each antenna is composed by a reflector, feed, transmission line and receiver. Credit: ALMA (ESO/NAOJ/NRAO)

1.3.2 Radio interferometry

Even though the telescopes' resolution depends on their size according to equation 1.4, increasing their diameter is not the only way to improve the angular resolution. In fact, when combining signals from two radio antennas detecting the same source simultaneously through *interferometry*, it is the distance between them that counts for the angular resolution. This can be pictured as a big radio telescope with a certain diameter being synthesised by two smaller telescopes at the distance from each other corresponding to the bigger telescope's diameter. Thus the resolution improves with the increase of the maximum distance between telescopes, which is called *baseline* (B). Furthermore, the more antennas are added so that there are more baselines with different lengths, the more information is obtained about the source's structure. Hence, the technique of *aperture synthesis* is of great importance when considering telescopes positions, specially when they are portable and need rearrangement [3].

In interferometry, the signals originated by the diffracted radio waves captured by two antennas simultaneously pointing at the same direction are correlated and the coherence of their signals measured, which is equivalent to the *visibility* of the diffraction fringes. This visibility, $V(u,v)$, is measured at the plane perpendicular to the radio propagation that can be called U-V plane. It can be converted to a real "image" of the source brightness, $I(x,y)$, by calculating the inverse Fourier transform of a quantity that includes the response of each individual antennas, $A(x,y)$, the source coordinate offsets (x,y) from the pointing direction of the telescopes and the baselines at the U-V plane. The expression of the visibility is then

$$V(u,v) = \iint_{source} A(x,y) I(x,y) \exp\{i2\pi(ux+vy)\}\, d(x,y). \tag{1.5}$$

It is also important to note that when the maximum distance between the antennas is increased, the resolving power of the interferometer improves, leading to the detection of smaller details according to the equation 1.4. But at the same time, larger structures are poorly imaged or even invisible [4, 5].

The most expensive radio mm/sub-mm interferometer of the present time, arguably also the most powerful, is the **Atacama Large Millimeter/submillimeter Array**, ALMA. It is located in the northern Chile's Atacama desert at an altitude of 5.000 meters above sea level and working since 2013 March. Its main array is composed by fifty antennas, each 12-metre in diameter and weighing over 100 tonnes, that when fully operational will detect wavelengths ranging from 0.3 mm to 9.6 mm. Additionally, they possess high mobility and can be spread in different configurations at distances of 150 metres to 16 km from each other with millimetre precision. This makes ALMA fully adaptable to different scientific goals. At the maximum baseline of 16 km and at observation wavelength of $\lambda = 0.3$ mm, a resolution of 0.004 arcseconds can be reached [6], which allow us to detect some of the farthest objects currently known, such as quasars and blazars.

1.4 The system PKS 1830−211

Radio–loud quasars make to a small percentage of the quasars' population, from which only a few present jet emission towards Earth. Even more rare is to find such blazars aligned with massive foreground objects, so that they are strongly gravitational lensed. In this context, the blazar PKS 1830−211 happens to be a treasure in the sky and its properties are analysed in this chapter.

The PKS 1830−211 is a radio-loud blazar at redshift z=2.507, which corresponds to a comoving radial distance of roughly 20,854 Mpc. It is a flat-spectrum radio quasar magnified due to the gravitational lensing effect of a gas-rich face-on spiral galaxy at redshift z=0.89, equivalent to 5,799 Mpc. There is a second galaxy aligned with these objects, which lensing effects are negligible compared to the $z = 0.89$ one.

Various observations of the blazar PKS 1830−211 in the cm-wave range have led to the detection of two core images connected by a pseudo-Einstein ring, similar to Figure 1.5 which was collected with the Multi-Element Radio Linked Interferometer Network (MERLIN). Both core images are separated by 0.98" and hereafter referred to as northeast (NE) or southwest (SW) image due to their relative positions. As the pseudo-Einstein ring presents a very steep spectral index compared to the main images, it becomes undetectable at mm/sub-mm. At the same time, the NE and SW images are magnified by a factor of 5-6 and 3-4 respectively at all frequencies [19]. The NE images is the leading one.

This particular gravitational lens is a quite rare object, as molecular absorption of background emission in gravitational lensing galaxies has been found in only two cases, the other one being B 0218+357 [20, 21]. Furthermore, gravitational lensing systems can contribute to the study of the cosmic microwave background radiation (CMBR) at different redshifts, the understanding of dark matter, jet physics and cosmological probes.

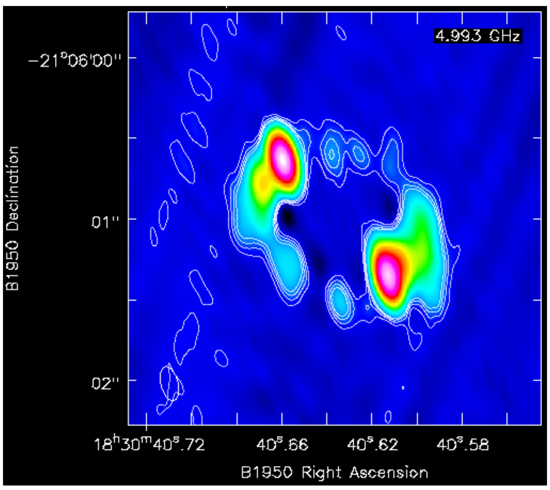

Figure 1.5: MERLIN image of PKS 1830−211 at C band, observed in year 1991 (and re-processed by team in Onsala). Two core images embedded in a pseudo-Einstein ring are observable.

Previous studies on the time delay

In this section three relevant techniques and results from previous studies on the time delay between the core images of the PKS 1830−211 are presented. The first study is from 1998 and analysed data in the radio band collected by the Australia Telescope Compact Array (ATCA) to conclude a time delay of $\Delta t = 26^{+5}_{-4}$ days [22]. The second study, from 2001, distinguished the molecular absorption of each light curve when passing through the foreground galaxy and found a time delay of $\Delta t = 24^{+5}_{-4}$ days [23]. Finally the most recent study, from 2011, determined a time delay of $\Delta t = 27.1 \pm 0.6$ days from the analysis of γ−ray light curves monitored by the *Fermi* Large Area Telescope, Fermi-LAT [24].

A. Radio emission with ATCA

This paper was a collaboration between J. Lovell, D. Jauncey, J. Reynolds, M. Wieringa, E. King, A. Tzioumis, P. McCulloch and P. Edwards. It was published in the Astrophysical Journal in 1998 November with the title "The Time Delay in the Gravitational Lens PKS 1830−211" [22].

Data Measurements of the flux densities of the NE and and SW components were collected every 3-6 days, between 1996 July and 1998 July, with the Australia Telescope Compact Array, ATCA, at 8.6 GHz. The flux density is overall increasing smoothly, except for a small bump of 400 mJy[1], during 1997 September.

Method At 8.6 GHz, the ATCA's resolution of 0.9" did not fully resolved the NE and SW components from the Einstein ring. Therefore, the first step was to determine the flux densities of each main core by modelling the data with two circular Gaussians accounting for the constant contribution of the Einstein ring. Then, the time delay was calculated using the dispersion technique from Pelt [25], which consists of correlating both light curves, shifting one with respect to the other by a certain time τ and calculate the statistical dispersion. The time delay should correspond to value of τ for which the statistical dispersion is minimum [25, 20]. Since this technique does not require the interpolation of unevenly distributed data, the chances of obtaining incorrect results decrease

In the analysis performed, the subscripts 1 and 2 correspond to the NE and SW images, respectively. The SW flux, $S_2(t)$, was expected to present the same shape as the NE flux, $S_1(t)$, but time shifted by $\Delta\tau$ and magnified by $\frac{1}{\mu}$. At the same time, the authors assumed different contributions of the Einstein ring for each of the core components, so that $S_{ring} = S_{c1} + S_{c2}$, where $S_{c1,2}$ are the unknown constant contributions and their difference gives the variable d. The measured SW flux, $S_{m2}(t)$, was then modelled by the equation

$$\begin{aligned} S_{m2}(t) &= S_2(t) + S_{c2} \\ &= \frac{1}{\mu} S_1(t + \Delta\tau) + S_{c2} \end{aligned} \tag{1.6}$$

[1]Jansky is a non-SI unit of spectral flux density, equivalent to 10^{-26}J s^{-1} m^{-2} Hz^{-1}.

and an estimation for the variables $\Delta\tau$, μ and d were found to be optimised at the minimum dispersion.

Results At minimum dispersion, the parameters fitted to the data resulted in $\Delta\tau = -23 \pm 4$ days, $\mu = 1.52 \pm 0.02$ and $d = -0.62 \pm 0.06$ mJy. When performing the same method on artificial NE and SW light curves similar to the original data, the robustness of the method was confirmed with the values $\mu = 1.52 \pm 0.05$ and $d = -0.62 \pm 0.05$ mJy, while $\Delta\tau$ showed a broad distribution between 12 and 30 days, with peaks around 15, 23 and 28 days. The same method was also performed only on data concerning the small outburst of 1997 September, with the purpose of better constraining the time delay. This was based on previous conclusions that smooth light curves can lead to poor results and ambiguous solutions of $\Delta\tau$. The results were $\Delta\tau = -26^{+5}_{-4}$ days, $\mu = 1.68$ and $d = -1.12$ mJy.

B. Molecular absorption

The next paper is named "Time Delay of PKS 1830−211 Using Molecular Absorption Lines", was written by T. Wiklind and F. Combes and published in the Astronomical Society of the Pacific Conference Series, in 2001.[23]

Most of the optical radiation coming from the lensed PKS 1830−211 is heavily extinct due to dust absorption in the interstellar medium. Moreover, it has been previously proven that the absorption lines of HCO^+ in the continuum spectrum is linked to the SW core component and therefore can be used to determine its continuum flux if heavily saturated, which is the case.

This paper takes advantage of this scenario and determines the time delay between both images with spectroscopy, which turns out to be more efficient in terms of time and resources than interferometry, because it only requires a low angular resolution single-dish telescope.

Data In 1996, 1997 and 1998, from around March to October, data regarding the total continuum flux and the depth of the absorption line of HCO^+ was collected by the Swedish-ESO Sub-millimetre Telescope (SEST).

Method The flux density of the SW component can be directly measured from the absorption depth of HCO^+ (2-1) lines. So the NE flux density can be later inferred from the total continuum flux. After correlating the NE and SW flux density curves according to the minimum dispersion analysis, or Pelt method [25, 20], the time delay was calculated.

Results The time delay found was $\Delta t \approx 24^{+5}_{-4}$ days.

C. γ-rays with *Fermi* LAT

The following paper, "First evidence of a gravitational lensing-induced echo in gamma rays with *Fermi*-LAT", was published in 2011 January in the Astronomy and Astrophysics Journal by A. Barnacka, J.-F. Glicenstein and Y. Moudden[24].

The *Fermi*-LAT is a high-energy telescope orbiting around Earth. It performs daily surveys of high-energy sources such as pulsars and active galactic nuclei.

In the high-energy gamma range, the core components of the gravitational lensed image of PKS 1830−211 cannot be resolved by the current technology. While the separation between NE and SW is 0.98″, the resolution provided by these instruments is a few arcminutes, at most.

Two solutions are presented to deal with spatially unresolved data. The traditional method is to apply the autocorrelation function to data, whereas this paper investigates the so-called "double power spectrum" method, which is used in fields like seismology and speech processing.

Data The data were collected between 2008 August and 2010 October by the *Fermi* LAT telescope at energies between 300 MeV - 300 GeV. The time sampling was two-day binning.

Method According to the article, the total observed brightness in time domain, $g(t)$, is the sum of the intrinsic brightness of the AGN and itself, accounting with a shift in time, a, and a magnification factor, b: $g(t) = f(t) + bf(t + a)$. The measured power spectrum, P_ν, is then obtained by computing the square modulus of the Fourier Transform of $g(t)$, which results in the product of the "true" power spectrum and a periodic component that depends on the time delay, as it can be seen in the equation

$$P_\nu = |\tilde{g}(\nu)|^2 = |\tilde{f}(\nu)|^2(1 + b^2 + 2b\cos 2\pi\nu a) \tag{1.7}$$

Assuming $|\tilde{f}(\nu)|^2$ as a constant function of ν, P_ν should present a peak at the time delay, a.

Results The method was tested on an artificial power spectrum with a known time delay of 28 days. The result obtained for the control test was $a \approx 28.35 \pm 0.56$ days, while the autocorrelation presented $a \approx 27.85 \pm 0.14$ days. Applying the same techniques to real data resulted in $a_{dbs} \approx 27.1 \pm 0.6$ days and $a_{ac} \approx 27.1 \pm 0.45$ days for the double power spectrum and autocorrelation methods, respectively.

Comment The data from this article was studied by other researchers and the conclusions drawn were conflictual. They found the blazar to be at quiescent state in the high-energy range and suggested that the original article had detected the Moon's $\gamma-$ray emission, and therefore calculated the period of the Moon's epicycle instead [19].

1.5 Aim of the master's thesis

In 2012, ALMA data were collected with the goal of studying the spectral absorption lines of the interstellar medium of the lensing galaxy at z=0.89, taking advantage of the blazar PKS 1830−211's continuum spectrum as background. The data revealed an unexpected variability of the flux ratio of the NE flux over the SW flux, both in time and frequency. After comparing the variability in radio and gamma wavelength collected by the telescope *Fermi*-LAT, which monitors the blazar on a daily basis, a strong γ-ray flare was detected at the same time as the radio measurements. And thus a possible correlation between the γ-ray flare and the strong emission in radio wavelength was established [26]. Later in 2014 more data were acquired with the purpose of studying the molecular absorption.

In this project, both the new data from 2014 and with the previous one from 2012 are analysed with two main purposes. The first one is to obtain the time delay between the core images NE and SW for a better constraint of the gravitational lensing model. The second goal is to derive some properties of the radiation inherent to the blazar (namely, spectral index and intrinsic light curve) from which several conclusions about the jet physics can be obtained.

2

Methodology

This chapter describes the techniques applied to the data collected by ALMA with the aim of determining the time delay between the NE and SW core images of PKS 1830−211. The study of flux density and flux ratio evolution of the blazar during two different activity states, quiescent and outbursting, is explored to also derive the spectral indices in 2012 and 2014 through numerical methods.

2.1 Data

The figures 2.1 and 2.2 show the measurements of the NE image flux density and flux ratio between both components, NE image flux over SW flux, during two periods, in 2012 (between 6020 and 6100 MJD[1]) and 2014 (between 6760 and 6900 MJD). The observed bands were 3, 6 and 7 which correspond to frequencies in the ranges 84 - 119 GHz, 211-275 GHz and 275-370 GHz, respectively. It is noticeable a sparse and uneven distribution of measurements for each band, which requires spectral index correction.

The data from the first period between 2012 April 09 and 2012 June 15 is composed by 14 epochs. Due to the relatively constant flux ratio distribution at around 1.4, this period was assumed to correspond to the quiescent state of the blazar, when the blazar's emission is minimum at radio band in this case. Later between 2014 April 24 and 2014 August 27, both the NE flux and the flux ratio rise as seen in the same Figures 2.1 and 2.2, sampled with 19 epochs. This is a strong indicator of activity in the blazar.

For both sets of data, the standard uncertainty associated to the flux density measurements is around 10-20%, whereas the uncertainty of the flux ratio is roughly 0.1%.The reason for this significant difference is that systematic errors, such as atmospheric absorption or receiver's response, affect the NE and SW images equally, so all these effects are removed from the flux-density ratio. Therefore, the NE flux intensity and the ratio fluxes of the NE over SW measurements are chosen to be studied in this thesis.

[1]The Modified Julian Date, MJD, is primarily used in Astronomy and is a modification of the Julian Day dating, JD, in the form of: MJD = JD - 2400000.5. The Julian day is a continuous count of days since the beginning of the Julian Period.

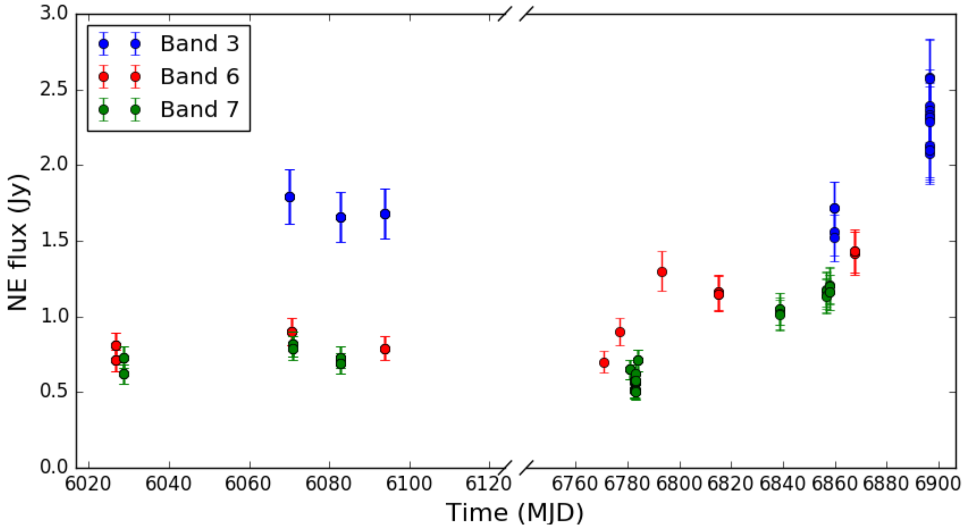

Figure 2.1: Raw data of the evolution of the NE image flux density of PKS 1830−211 collected with ALMA in 2012 and 2014. The NE flux density was quite steady in 2012 (between 6020 and 6100 MJD), while it dramatically increased in 2014 (between 6760 and 6900 MJD).

2.2 Method

Considering the NE flux intensity (F_{NE}) and flux ratios ($R = F_{NE}/F_{SW}$) at certain frequencies (ν) and epochs (t) of PKS 1830−211, a method to determine the time delay (τ) between the core images of the blazar was set forth, starting with the spectral index correction and moving on to determining the light curve of NE$(t - \tau)$ based on NE(t), as sketched in the Figure 2.3. The spectral index correction is an essential step in order to be able to compare the NE fluxes at different bands. Thus, they must first be scaled to the same fiducial frequency, for example, 100 GHz.

2.2.1 Spectral index correction

As describe by the flow chart in Figure 2.3, the first part of the analysis was the correction for the spectral indices in 2012 and 2014, α_{12} and α_{14}. They were expected to be potentially different due to the large time span between both sets of measurements relatively to the time scale of the blazar's variability. Once the spectral indices were found, data were corrected taking into account that the fluxes were approximately constant in 2012 and increasing in 2014.

A. 2012 Data

In 2012, small variations of the NE fluxes and ratios imply that the blazar was almost at the quiescent state in mm/sub-mm wavelength, with low radio flaring mode. It was then assumed that each measured NE flux during this period actually corresponded to the uncorrected blazar's absolute flux, the fiducial flux (F_0), at a certain reference frequency ν_0. In order to find the absolute flux, the data were linearised by working in logarithmic scale and the function `(data - model)` was

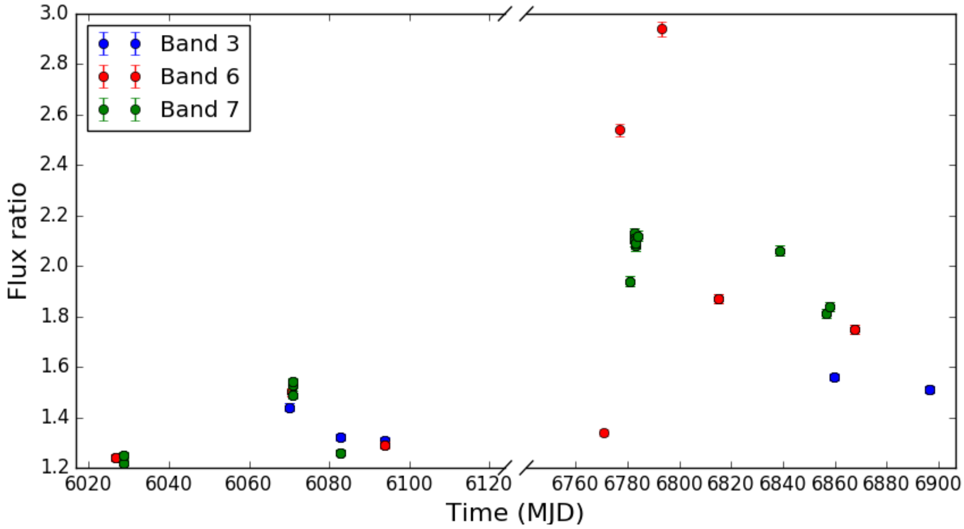

Figure 2.2: Flux ratio evolution of PKS 1830−211 observed with ALMA during 2012 and 2014. The flux ratio varies in a wide amplitude range in 2014. A substantial decrease of the error bars is also clear when performing the flux density ratio, due to the automatic exclusion of systematic errors that affect both NE and SW components.

then minimised using the `Python/Scyipy` built-in numerical method of the standard least squares fitting `scipy.optimize.leastsq`. The linearisation of data assured the best performance of the algorithm. Then, the definition of spectral index was used as a model, as

$$F = F_0 \left(\frac{\nu}{\nu_0}\right)^{\alpha} \ . \tag{2.1}$$

The input arguments were the measured F_{NE12} and corresponding frequencies ν_{12}, while the output fitting parameters were the spectral index α_{12} and the fiducial flux $F_{0,12}$, at a reference frequency, ν_0, defined by the user, as for example 100 GHZ.

B. 2014 Data

Only after determining the quiescent flux ratio in 2012, was it possible to correct the data in 2014. As the blazar was in outbursting state at this time, we assumed a decoupling of frequency and time dependence of the flux evolution in the form of

$$F(t, \nu) = G(\nu) \cdot H(t) \ , \tag{2.2}$$

with $G(\nu)$ corresponding to equation 2.1 and $H(t)$ taking the form of a linear function to simplify, as $H(t) = m * (t - t_0)$. The variable t_0 accounts with the possibility that the radio flare became visible on Earth some time after the monitoring of PKS 1830−211 had already started, so that there is a mixture of quiescent state and flare mode in the 2014 data.

It followed once more the linearisation and minimisation of the expression `(data - model)` using the `Python/Scipy` function `scipy.optimize.leastsq` to obtain the spectral index, α_{14} and the linear function parameters, m and t_0. The input arguments were the reference frequency, F_0, the NE flux density, F_{NE14} and

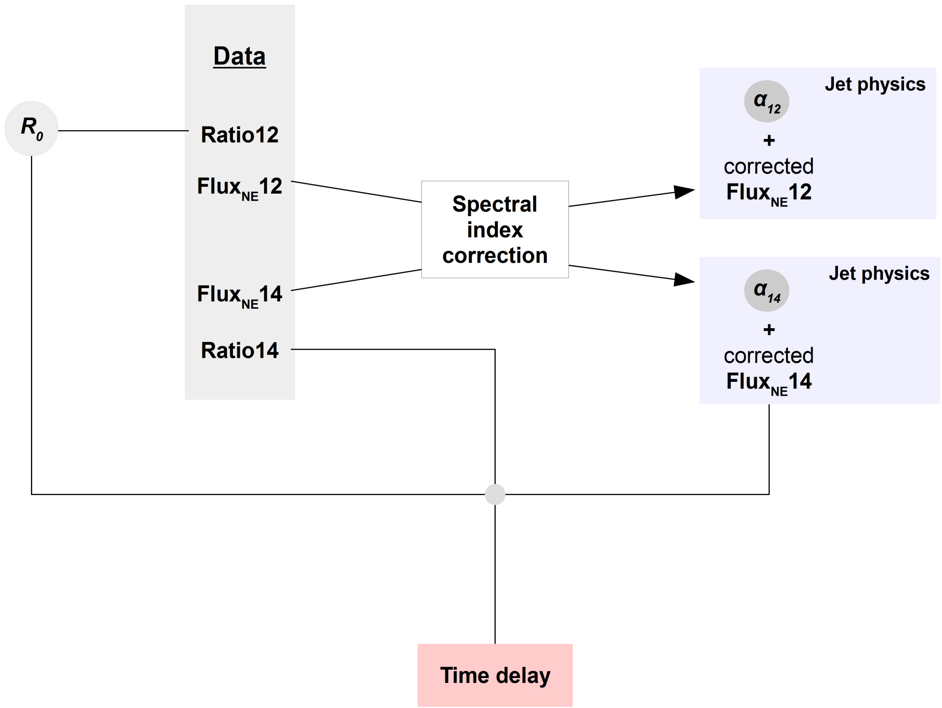

Figure 2.3: Flow chart of the experimental method with two goals: determination of the time delay between lensed images and the qualitative study of the jet physics. The data taken in 2012 and 2014 are identified with "12" and "14", respectively.

the respective frequencies and epochs. The reference frequency was chosen as in 2012, so that all data could be compared relatively to the same frequency reference after correction.

2.2.2 Time delay

Once the data in 2014 was corrected, new values of NE fluxes corresponding to the time $t - \tau$ could be derived from the SW lightcurve detected at t. In order to understand the relation between time delay, observed flux ratio and quiescent flux ratio, a timeline of PKS 1830−211 activity was sketched in Figure 2.4. Initially the blazar is at quiescent state and its radio emission is constant, with a quiescent flux ratio of R_q and NE lightcurve reaching Earth at a certain time τ earlier than the SW counterpart. Then at time t_{em} a flare is emitted by the blazar and the disturbance from the quiescent state is first detected by the leading image NE at t and later in the SW image at $(t + \tau)$, with the same variation but different magnitude.

Even if the flare extinguishes, these different states of the blazar can be inferred by the study of its flux ratio. For example, if the blazar's activity rises, the NE flux increases, $F_{NE}(t + \tau) > F_{NE}(t)$. As SW flux remains the same due to the time delay, there is an increase of the ratio flux $R(t) > R(t - \tau)$. On the opposite side, if the blazar's flare starts to fade away, following the same way of thinking, $NE(t + \tau) < NE(t)$ so $R(t) < R(t - \tau)$. Finally, in case of constant emission, as at quiescent ratio, the flux ratio does not change, $R(t) = R(t - \tau)$, and its value shows

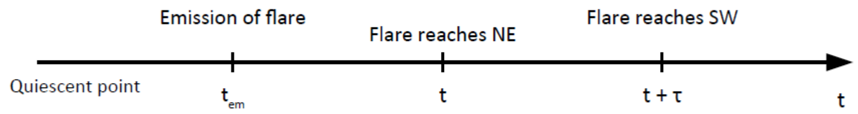

Figure 2.4: Timeline of flare emitted by a certain gravitationally lensed object at time t_{em} and detected on Earth at different times t and $t+\tau$ by each of the lensed images.

the relative magnification of NE and SW images.

It should be noted that the quiescent flux ratio, R_q, is the differential magnification between the NE and SW images, which are constant and arise purely due to the geometry of the gravitational lens. Therefore, R_q does not change with time (considering that the relative positions of the blazar, galaxy and Earth remain constant) and can be interpreted as the fixed relation between the NE flux and the delayed SW flux for the same state of the quasar. For example, once a flare is detected in the leading NE image, it takes the time τ for the SW component to be updated. So the NE flux at the moment the flare is detected, $t-\tau$, over the SW flux at the time the same event is detected, (t), is the quiescent flux ratio, R_q, as written in the first equation in 2.3. By combining this equation with the definition of flux ratio at $(t+\tau)$, it became possible to acquire information about past events from the data collected at t, as shown in equation

$$\begin{cases} R_q = \dfrac{F_{NE}\,(t-\tau)}{F_{SW}\,(t)} \\ \\ F_{SW}\,(t) = \dfrac{F_{NE}\,(t)}{R(t)} \end{cases} \Longrightarrow F_{NE}\,(t-\tau) = \frac{R_q}{R(t)} \cdot F_{NE}\,(t) \tag{2.3}$$

It then became clear that the time delay between the NE and SW components could be determined by calculating τ between the fluxes NE at t and NE at $(t-\tau)$. While the NE flux at t was given directly by the data, the NE flux at $(t-\tau)$ could be obtained from the flux ratio at quiescent state, NE flux and ratio flux at t.

As the blazar was at quiescent state in 2012, R_q was determined by considering that all measurements of the flux ratio in 2012 corresponded to the quiescent flux ratio. Therefore all the flux ratio measurements from this date were averaged as $R_q = < R_{12} >$.

Because of the blazar's outburst, the measured flux ratio evolution in 2014 is variable, which is the only condition needed to find a time delay between two identical curves shifted in time. So the second set of data $F_{NE,14}(t-\tau)$ was calculated from the measurements of NE flux densities and flux ratios in 2014, according to the equation 2.3. When plotting flux density in function of time, it was expected to find the new set of delayed points presenting a similar shape to $F_{NE,14}$, but affected by a time shift.

There were two implementations of the same minimisation method to determine the time shift between $F_{NE,14}$ and $F_{NE,14}(t-\tau)$. The first one was fitting polynomial curves to both sets of data assuming equal parameters and accounting with a variable for the time delay, according to the equation

$$f(t) = a + b(t-\tau) + c(t-\tau)^2 + ... \tag{2.4}$$

The fitting was then performed with the `Python` function `scipy.optimize.leastsq`, which concatenated both models because of the common parameters $a, b, c....$ In this way, all parameters and data could influence and be influenced by all the others, increasing the accuracy of the result. The output values were then the parameters of the fitting curve and τ.

In the second method, the polynomial curves used in the previous method were applied with the difference that the time delay τ was fixed to a given value. The `Python` function then calculated the free parameters of the polynomial curve and its reduced chi-square for each defined time delay, that varied from 10 to 50, with half a day increments. In the end, there was a plot of the reduced chi-square in function of the pre-defined time delays for each polynomial curve that were compared.

2.3 Implementation details

For the analysis of data, the general programming language `Python` was used due to its libraries oriented for scientific and numeric computing, such as: `SciPy`, `NumPy` and `Matplotlib`. In summary, `SciPy` provides easy-to-implement numerical routines, like integration and optimization, `NumPy` provides a vast range of tools to manipulate numerical arrays and matrices and finally `Matplotlib` supports plotting. For more information, the Python Software Foundation has made available the `Python` Language Reference, for version 2.7.

The described method can be divided in five parts, as sketched in figure 2.5: the main execution script `main.py`, the spectral indices calculation `spectralindex.py`, the time delay calculation `tdelay.py`, the data plotting `plots.py` and the auxiliary functions `functions.py`. The routines used for each calculation are also specified in the figure.

The script starts by organising the data according to its year with `arr_data()` and creates masks that differentiate their three different bands with `bands()`. Then the data from 2012 is used to calculate the spectral index with `spectral12()` and the value found is confirmed after performing a Monte-Carlo simulation with fluxes varying within their error bars, at `mc_propag()`. After the quiescent ratio is calculated in `main.py`, the spectral index for 2014 is calculated and tested using `spectral14()` and `mc_propag()` respectively. Finally with the corrected NE fluxes and quiescent ratios, together with the epochs and flux ratios, the time delay between images is calculated through two different methods, `free_tau()` and `chisq()`. In the end, plots of the data and of the chi square present the results in a more visual way with `plt_flux()` and `plt_chisq()`.

The `functions.py` script also contains auxiliary routines to perform and plot the least-squares fitting `scipy.optimize.leastsq`, such as the definition of functions and labels.

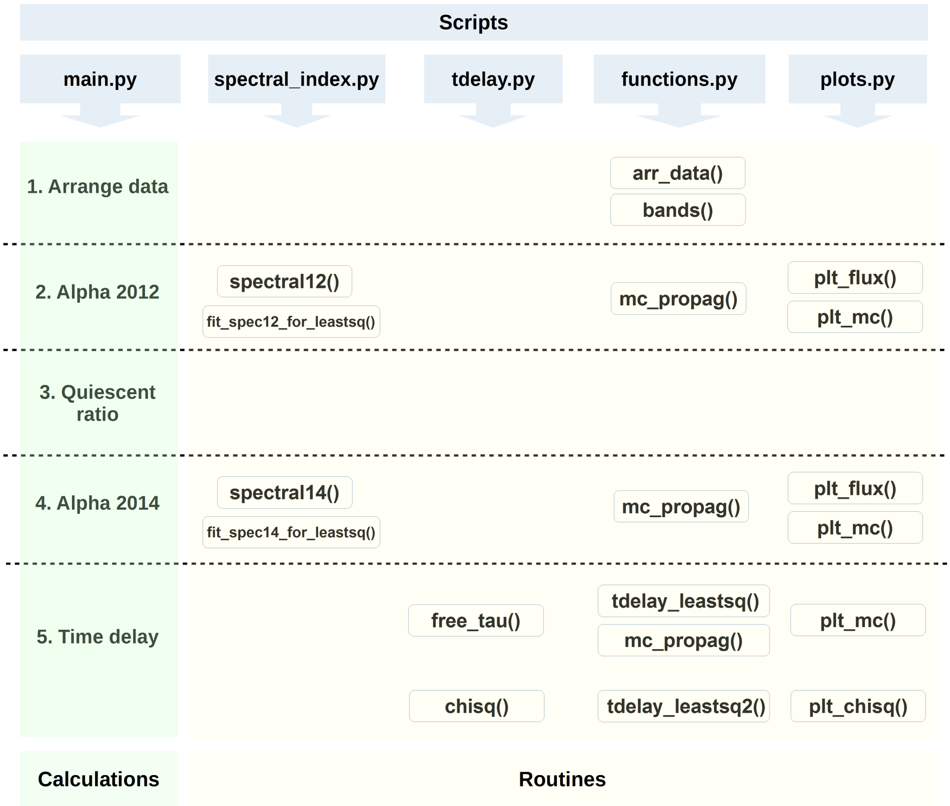

Figure 2.5: Architecture of algorithm implemented in `Python`.

3

Results

This chapter presents the results obtained for the spectral indices in 2012 and 2014 and the time delay between NE and SW images, using the methodology described in the previous chapter.

The plots in Figure 3.1 and 3.2 show the NE fluxes as a function of frequency (upper subplot) and time (middle plot), as well as the flux ratios as a function of time together with the quiescent flux ratio (lower subplot), for both periods in 2012 and 2014. In both cases, the assumed fiducial frequency was 100 GHz.

In 2012, a low variation of the corrected flux ratio is visible, between 1.2 and 1.6, and thus this spectrum is considered to reflect the quiescent state of the blazar. An interesting consequence of the spectral index correction is the flatness of the spectrum, with the NE flux averaging around the value 1.68 Jy. We found the spectral index to be $\alpha_{12} = -0.77 \pm 0.03$, the fiducial flux $F_{0,12} = 1.67 \pm 0.05$ Jy and the quiescent ratio, $R_0 = < R_{12} > = 1.35$.

On the other side, in 2014, both the evolution of the NE flux and the flux ratio contrast with the steady tendencies identified in 2012. Not only is visible that the NE flux density is varying from around 0.7 Jy to 2.5 Jy, but also the flux ratio exhibits a small bump at around 6780 MJD, decreasing afterwards, but still higher than R_0. We found the spectral index to be $\alpha_{14} = -0.35 \pm 0.09$ and the parameter $F_{0,14} = 0.28 \pm 0.26$.

The uncertainties for the spectral indices and fiducial flux ratios for both years were determined by Monte Carlo simulation and the histogram of the simulations is shown in figures 3.3 and 3.4 for 2012 and 2014, respectively. The simulations were run for 100,000 times for each year and the data distributed in 500 bins.

Finally for the estimation of time delay, both implementations present similar results. By letting the time delay, τ, behave a free parameter, we obtained values between 20 and 28 days, as shown in table 3.1. When performing the Monte Carlo simulation for the specific case of a second degree polynomial, we obtained the histogram 3.6, which average and standard deviation give a time delay of $\Delta t = 28 \pm 3$. Consistent results were obtained when calculating the minimised chi-square for each predefined time delay, which varied from 10 to 50 days with increments of 0.5 days, and for each polynomial fitting the data. Figure 3.5 shows the five chi-square curves in function of a fixed time, for each of the five fitting polynomials. Each curve has the minimum of the chi-square at around 28 days.

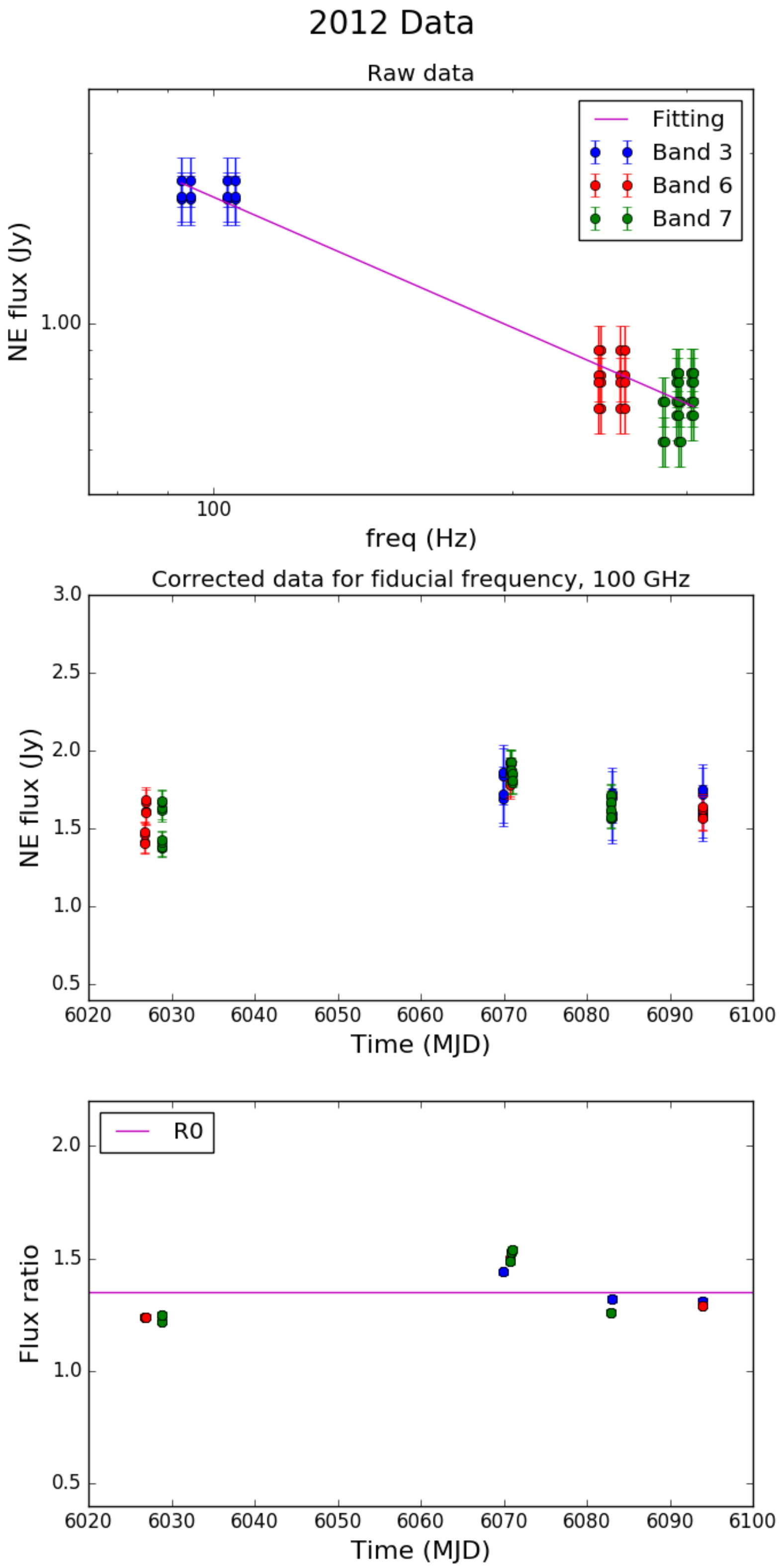

Figure 3.1: Data from 2012. The upper plot shows the raw data of NE flux density as a function of frequency. The middle one presents the NE flux density corrected for the fiducial frequency 100 Ghz as a function of time. The bottom plot shows the flux ratios as a function of time, together with the quiescent flux ratio. This data corresponds to the quiescent state of the blazar.

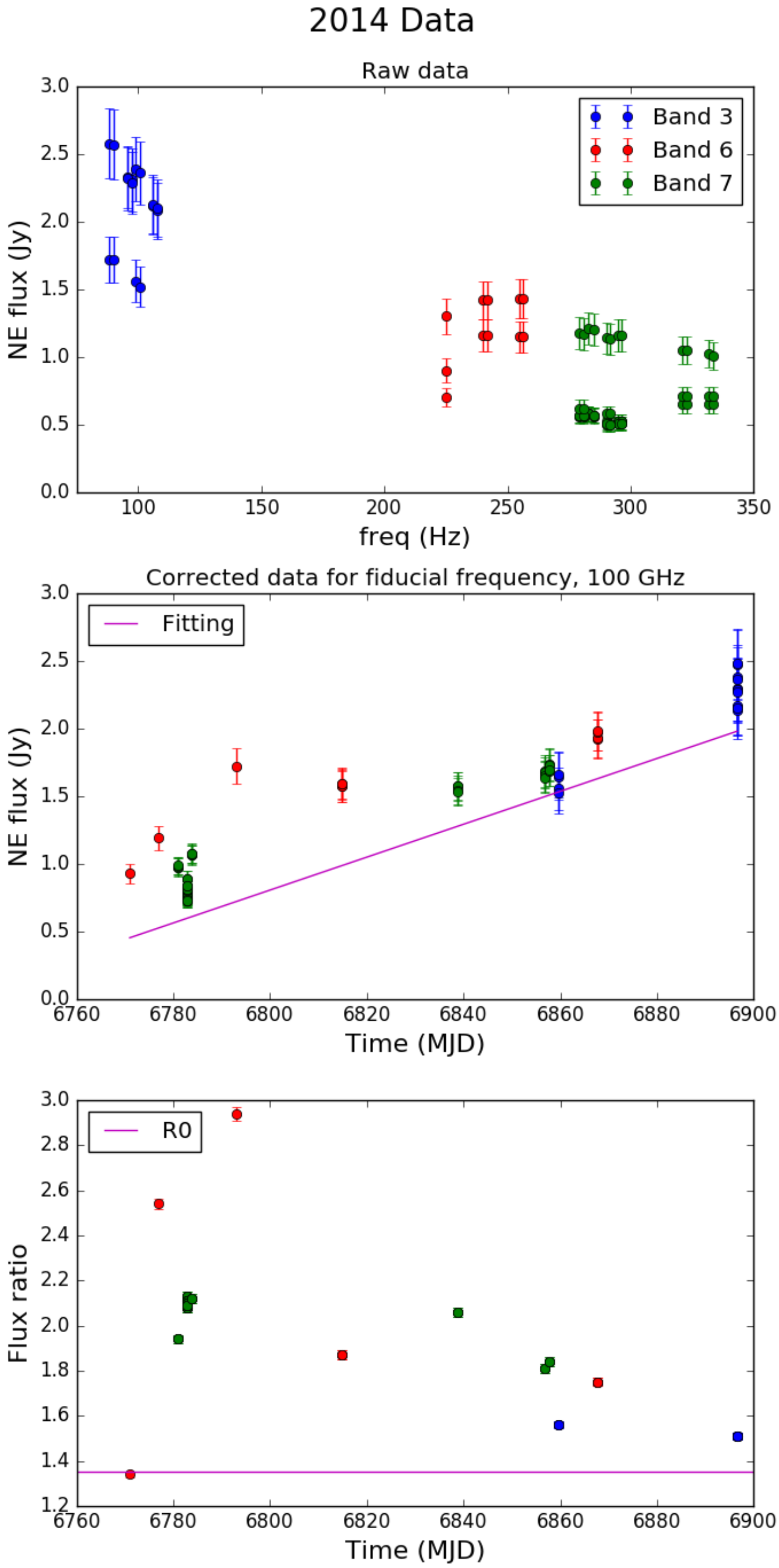

Figure 3.2: Data from 2014. The upper plot shows the raw NE flux density as a function of frequency. The middle one presents the corrected NE flux density as a function of time, together with the best fitting curve. The plot in the bottom shows the flux ratios as a function of time. An outburst is observable in the blazar.

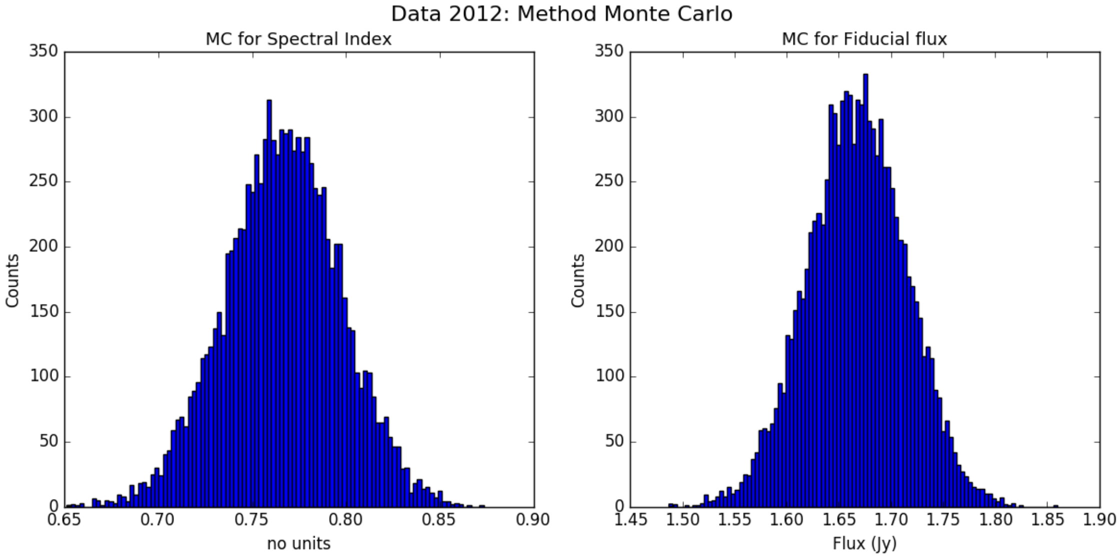

Figure 3.3: Data from 2012: Monte-Carlo simulation to determine the spectral index, α_{12}, and the fiducial flux. The algorithm was run for 100,000 trials and the results distributed in 500 bins. The values found for the spectral index and fiducial flux were $\alpha_{12} = -0.77 \pm 0.03$ and $f_{0,12} = 1.67 \pm 0.05$ Jy.

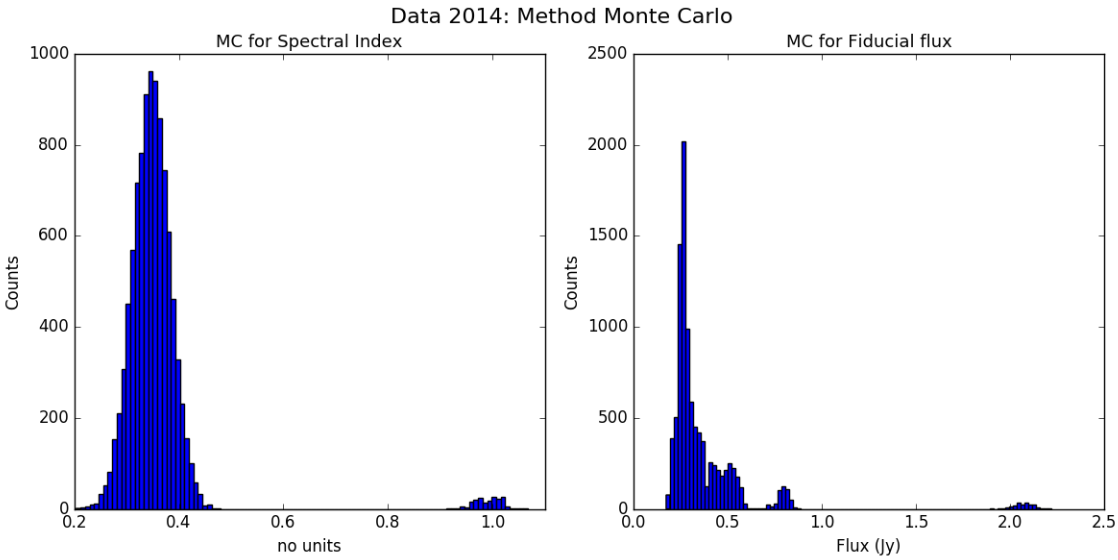

Figure 3.4: Data from 2014: Monte-Carlo simulation to determine the spectral index, α_{14}, and the fiducial flux. The algorithm was run for 100,000 trials and the results distributed in 500 bins. The values found for the spectral index and fiducial flux were $\alpha_{14} = -0.35 \pm 0.09$ and $f_{0,14} = 0.28 \pm 0.26$ Jy.

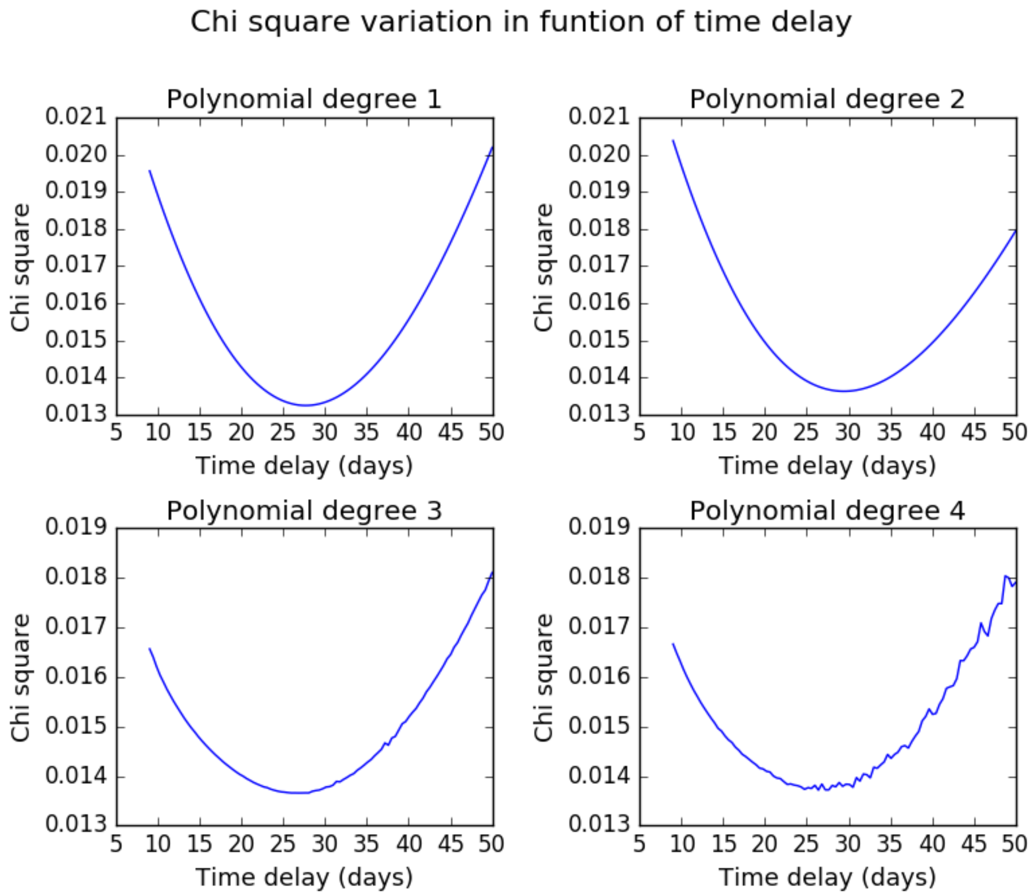

Figure 3.5: Determination of the time delay by finding the minimised chi-square value given a fixed time delay. This method was applied to 5 polynomials and each curve is constituted by 100 points equally spaced.

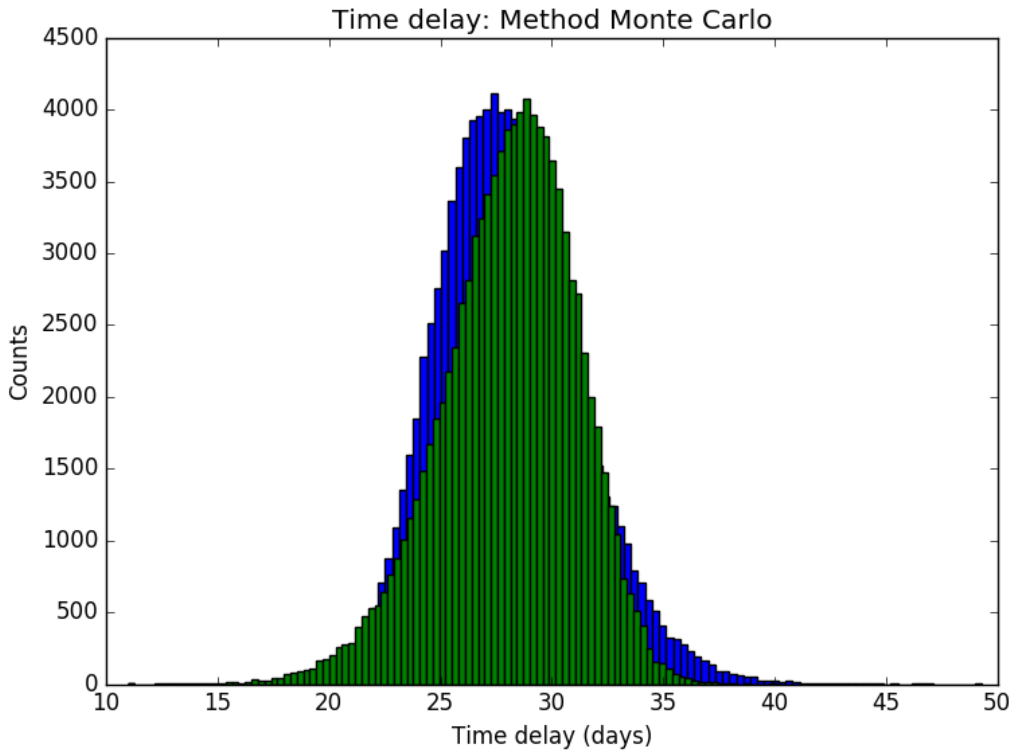

Figure 3.6: Monte-Carlo simulation to determine the time delay between the lensed images of PKS 1830−211. The blue histogram corresponds to the fitting of a linear function to the NE (t) and NE (t−τ) flux densities, whereas the green one corresponds to the fitting of a second degree polynomial. The algorithm was run for 100,000 trials and the results of the time delay distributed in 100 bins. For both fitting curves, the time delay found was $\Delta\tau = 28 \pm 3$ days.

Fitting light curve $H(t)$	Parameters	Time delay	Initial values
$h = a\ (t-\tau) + b$	$a = 1.20e-2$	$\Delta t = 27.78 \pm 5.25$	$\Delta t = 10$
	$b = -8.03e+1$		$a = 1$
			$b = 0$
$h = a\ (t-\tau)^2 + b\ (t-\tau) + c$	$a = 1.65e-5$	$\Delta t = 28.35 \pm 5.44$	$\Delta t = 10$
	$b = -2.13e-1$		$a = 1$
	$c = 6.88+2$		$b = 0$
			$c = 0$
$h = a\ (t-\tau)^3 + b\ (t-\tau)^2 + ...$	$a = 1.15e-7$	$\Delta t = 27.30 \pm 6.60$	$\Delta t = 10$
	$b = -2.34e-3$		$a = 1$
	$c = 1.59e+1$		$b = 0$
	$d = -3.60e+4$		$c = 0$
			$d = 0$
$h = a\ (t-\tau)^4 + b\ (t-\tau)^3 + ...$	$a = 6.30e-11$	$\Delta t = 24.00 \pm 5.77$	$\Delta t = 24$
	$b = -1.11e-6$		$a = 1$
	$c = 5.23e-3$		$b = 0$
	$d = 4.28$		$c = 0$
	$e = -5.51e+4$		$d = 0$
			$e = 0$

Table 3.1: Fitting parameters of polynomials functions used to determine the time delay between the NE(t) and NE($t-\tau$) light curves. The 4-degree polynomial failed in converging to the right result, always presented the initial value as final result.

4 Discussion

From the analysis of data, the determined time delay between lensed images was $\Delta t = 28 \pm 3$ days and the spectral indices were $\alpha_{12} = -0.77 \pm 0.03$ and $\alpha_{14} = -0.35 \pm 0.09$. In this chapter, the meaning and implications of these results are discussed and compared to previously reported results. Furthermore, some limitations of the methodology are pointed out.

4.1 Time delay

This is the first time that ALMA has been used to measure the time delay of a gravitational lens. And despite the uneven small amount of data measured at different bands, we found a value of $\Delta t = 28 \pm 3$ days for the time delay, a result that is in agreement with previous studies. We can also confirm the robustness of our result due to the consistent values obtained by two different implementations: by fitting the time delay simultaneously to the lightcurve parameters or by fixing it initially. Another interesting consideration was checking the performance of both algorithms when using the 4-degree polynomial for the modelling. While the method with time delay as free parameter saturated and always returned the initial condition as final solution, the second method succeeded in identifying the corrected time delay for the minimised chi square, regardless of the starting parameter values.

From the time delay between the core images it is possible to measure the Hubble constant and refine the lens model, which in turn would allow the study of the density distribution of dark matter surrounding the foreground galaxy. This is not straightforward however, and is beyond the scope of this thesis.

4.2 Spectral indices

Both periods present negative spectral indices, with values characteristic of non-thermal radiation, specifically synchrotron emission, which spectral index usually varies around $\alpha_{sync} \simeq -0.5$ as mentioned before. From 2012 to 2014 the spectral index decreased (in absolute value), which means that some event occurred causing such release of energy that opacity effects were overcome. At the same time the spectrum got flatter, there was an increase of the flux density in 2014, which is in agreement with the 2014 flux ratios measurements above the fiducial flux ratio. That implies a constant increase of the blazar's brightness, as seen in 2.2.2. This tendency can be explained by the outburst of a flare, that was continuously getting stronger, and therefore the SW image could not catch up the NE image to make the ratio go down. As to confirm this idea, a clear peak in the flux ratio arises at around 6780 MJD. Unfortunately none of the polynomials fitted to the light curves succeeded in describing this behaviour due to lack of data at precisely 27 days before, at 6753 MJD.

The spectral indices were calculated in a conservative regime by performing Monte-Carlo simulations, and therefore the non-linearities that could interfere with the calculations of the parameters from the minimisation of the chi square were overcome.

4.3 Gamma–ray flare counterpart

We compared the radio emission detected with ALMA and the gamma–ray emission detected by the *Fermi*-LAT during the same periods. The gamma-ray light curve in Figure 4.1 shows gamma-ray outbursts during the time of our mm/sub-mm observations in both 2012 (from around 6020 to 6100 MJD) and 2014 (from around 6760 to 6900 MJD). Also according to the zoomed plot, the clear peaks of gamma–ray flux densities present similar magnitudes. However, the response of the radio-flare counterpart was much stronger and noticeable in 2014 than in 2012. Even though small variations in both NE flux density and flux ratio are visible in 2012, we considered as being in radio range quiescent state. A possible explanation for the almost absence of radio counterpart in 2012 is that the origin of the radio flare in 2014 was the same as the gamma– ray flare, implying that the observations were very close to the base of the jet. It is possible then to consider that both flaring events analysed during the present thesis were caused either by different processes or in different regions of the jet.

4.4 Limitations

Despite the agreement of the presented results with the literature, there are some initial assumptions that could have lead to wrong results. For instance, it was assumed the quiescent state of the blazar during the three months monitored in 2012, but still small variations in data existed that gain importance due to the high accuracy of flux ratio measurements. In addition, the flux ratio were all larger than the quiescent ratio obtained from the modelling, which was around 1.35 ± 0.12.

Regarding the developed code, for educational purposes the determination of the different quantities presented (spectral indices, parameters of fitted functions and time delay for instance) was computed in a modular way, where routines gave outputs that served as input of the next routine. This means that the uncertainties were propagated alongside the results. A better way to proceed with the data in 2014 would have been to concatenate all the mentioned variables in only one routine, so that the respective uncertainties would have mutual influence on each other when using the `Python/SciPy` built-in function `scipy.optimize.leastsq`. In this way, the uncertainties could be slightly higher, but the results surely more robust.

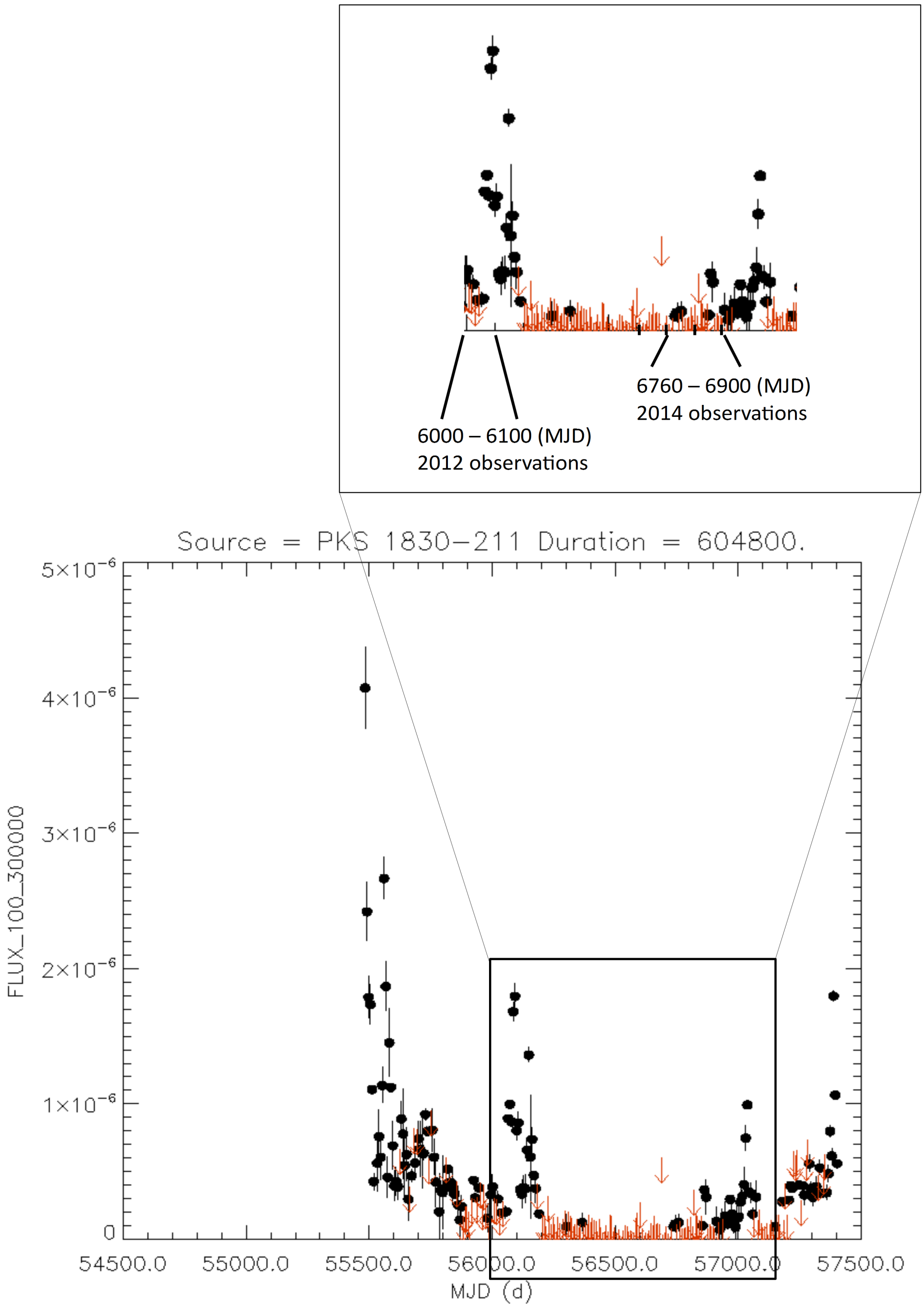

Figure 4.1: Gamma-ray light curve of PKS 1830−211, detected by *Fermi*-LAT on a daily basis during the period from 55500.0 to 57400.0 MJD (from n2010 October 31 to 2016 January 13).

5
Conclusion

Blazars are characterized by powerful highly directional outflows of energy. These seem to have origin in a nuclear rotating supermassive black hole that is surrounded by hot dense plasma in the accretion disk. The understanding of such distant objects have implications in cosmology, jet physics and theory of relativity. In addition, the gravitationally lensed blazar PKS 1830−211 allows the study of the molecular absorption of its lensing galaxy.

In this thesis the time delay between the lensed images of PKS 1830−211 was calculated with the aim of constrain its gravitational lensed model. With this value, together with other quantities like the galaxy's mass distribution, it is possible to calculate the Hubble constant, which is related with the age, size and expansion of Universe. This requires further work as it requires the application of parameterised models to describe the mass distribution the foreground's galaxy. Data from the NE image flux density and flux density ratios was collected with ALMA in 2012 and 2014, which corresponds to mm/sub-mm wavelength. The value found for the time delay was $\Delta t = 28 \pm 3$ days, which is in agreement with previous studies.

We have also identified two different activity modes of the blazar PKS 1830−211. While the blazar appeared to be in low radio flaring mode in 2012, the circumstances dramatically changed in 2014. Not only the absolute value of the spectral index decrease from 2012 to 2014 ($\alpha_{12} = -0.77 \pm 0.03$ to $\alpha_{14} = -0.35 \pm 0.09$), but also there was a time evolution of the NE flux density and flux ratio. This suggests the outburst of a strong radio flare in 2014. Interestingly, when compared the radio flux density from ALMA with the $\gamma-$ray monitoring by *Fermi*-LAT, we found that $\gamma-$ray flares were emitted during the time of our observations. While the radio outburst coincided with a gamma-flaring in 2014, there was no radio counterpart in 2012.

For the data analysis different techniques were used so as to increase the robustness of the results, such as optimization of the chi-square, Monte-Carlo simulations and the study of time delay as a free variable or predefined parameter. Despite the sparse and uneven data from three different bands, it was possible to determine a value for the time delay in agreement with previous studies.

For the future, a better sampling of data could make it possible to understand for sure when the blazar is at quiescent state. Then, the natural continuation of this thesis is the determination of the Hubble constant by combining the calculated time delay and other studies of the lens mass model. Finally, it could be interesting to analyse the spectral index in a wider range of frequencies in order to study the effects of chromaticity and the possibly different origins of radiation (close to the base of the jet or upper the stream).

Bibliography

[1] J. J. Condon and S. M. Ransom. *Essential Radio Astronomy. Introduction to Radio Astronomy*. National Radio Astronomy Observatory. Sept. 13, 2010. URL: http://www.cv.nrao.edu/course/astr534/Introradastro.html.

[2] Diane Fisher Miller. *Basics of Radio Astronomy for the Goldstone-Apple Valley Radio Telescope*. 1998. URL: http://www.jpl.nasa.gov/radioastronomy (visited on 01/2016).

[3] P. Karttunen et al., eds. *Fundamental Astronomy*. Fifth. Springer Berlin Heidelberg New York, 2007. ISBN: 978-3-540-34144-4. DOI: 10.1007/978-3-540-34144-4.

[4] K. Rohlfs, T.L. Wilson, and S. Huttemeister. *Tools of Radio Astronomy*. Sixth. Springer Berlin Heidelberg, 2013. ISBN: 978-3-642-39950-3. DOI: 10.1007/978-3-642-39950-3.

[5] G. L. Verschuur and K. I. Kellermann, eds. *Galactic and Extra-Galactic Radio Astronomy*. Springer Berlin Heidelberg, 1974. ISBN: 978-3-642-96178-6. DOI: 10.1007/978-3-642-96178-6.

[6] ALMA. "ALMA in-depth: how will ALMA make images?" In: *ALMA Newsletter* 5 (Apr. 2010). URL: https://almascience.eso.org/news/newsletters/newsletter-no.-5/view.

[7] A. Ferrari. "Modeling Extragalactic Jets". In: 36 (1998), pp. 539–598. DOI: 10.1146/annurev.astro.36.1.539.

[8] *Images of Radio Galaxies and Quasars: Quasar 3C175*. 2015. URL: http://www.cv.nrao.edu/~abridle/3c175.htm.

[9] I. Contopoulos, D. Gabuzda, and N. Kylafis, eds. *The Formation and Disruption of Black Hole Jets*. 2015.

[10] M. D'Onofrio, P. Marziani, and J. W. Sulentic, eds. *Fifty Years of Quasars: From Early Observations and Ideas to Future Research*.

[11] *title*. Jan. 2016. URL: http://hypertextbook.com/facts/2007/DanielTouger.shtml.

[12] A. R. Choudhuri. *Astrophysics for Physicists*. 5th ed. Cambridge University Press, New York, 2010. ISBN: 978-0-511-67742-7.

[13] P. F. Hopkins et al. "A Unified, Merger-driven Model of the Origin of Starbursts, Quasars, the Cosmic X-Ray Background, Supermassive Black Holes, and Galaxy Spheroids". In: 163 (Mar. 2006), pp. 1–49. DOI: 10.1086/499298. eprint: astro-ph/0506398.

[14] L. Mayer et al. "Direct formation of supermassive black holes via multi-scale gas inflows in galaxy mergers". In: 466 (Aug. 2010), pp. 1082–1084. DOI: 10.1038/nature09294. arXiv: 0912.4262.

[15] M. C. Begelman, M. Volonteri, and M. J. Rees. “Formation of supermassive black holes by direct collapse in pre-galactic haloes”. In: 370 (July 2006), pp. 289–298. DOI: 10.1111/j.1365-2966.2006.10467.x. eprint: astro-ph/0602363.

[16] A. O. Petters, H. Levine, and J Wambsganss. *Singularity Theory and Gravitational Lensing*. Ed. by Springer Science and Business Media New York. 21 vols. 2001. ISBN: 978-1-4612-0145-8. DOI: 10.1007/978-1-4612-0145-8.

[17] S. Refsdal. “On the possibility of determining Hubble’s parameter and the masses of galaxies from the gravitational lens effect”. In: 128 (1964), p. 307. DOI: 10.1093/mnras/128.4.307.

[18] R. D. Blandford and R. Narayan. “Cosmological applications of gravitational lensing”. In: 30 (1992), pp. 311–358. DOI: 10.1146/annurev.aa.30.090192.001523.

[19] A. A. Abdo et al. “Gamma-Ray Flaring Activity from the Gravitationally Lensed Blazar PKS 1830–211 Observed by Fermi LAT”. In: *The Astrophysical Journal* 799.2 (2015), p. 143. URL: http://stacks.iop.org/0004-637X/799/i=2/a=143.

[20] F. Courbin and D. Minniti, eds. *Gravitational Lensing: An Astrophysical Tool*. Springer, 2002.

[21] K. M. Menten, C. L. Carilli, and M. J. Reid. “Interferometric Observations of Redshifted Molecular Absorption toward Gravitational Lenses”. In: Astronomical Society of the Pacific Conference Series 156 (1999). Ed. by C. L. Carilli et al., p. 218. eprint: astro-ph/9812178.

[22] J. E. J. Lovell et al. “The Time Delay in the Gravitational Lens PKS 1830-211”. In: *Astrophysical Journal, Letters* 508 (Nov. 1998). Provided by the SAO/NASA Astrophysics Data System, pp. L51–L54. DOI: 10.1086/311723. eprint: astro-ph/9809301. URL: http://adsabs.harvard.edu/abs/1998ApJ...508L..51L.

[23] T. Wiklind and F. Combes. “Time Delay of PKS 1830-211 Using Molecular Absorption Lines”. In: Astronomical Society of the Pacific Conference Series 237 (Jan. 2001). Ed. by T. G. Brainerd and C. S. Kochanek. Provided by the SAO/NASA Astrophysics Data System, p. 155. eprint: astro-ph/9909314. URL: http://esoads.eso.org/abs/2001ASPC..237..155W.

[24] A. Barnacka, J.-F. Glicenstein, and Y. Moudden. “First evidence of a gravitational lensing-induced echo in gamma rays with Fermi LAT”. In: *Astronomy and Astrophysics* 528 (Apr. 2011). Provided by the SAO/NASA Astrophysics Data System. DOI: 10.1051/0004-6361/201016175. arXiv: 1011.4498. URL: http://esoads.eso.org/abs/2011A%26A...528L...3B.

[25] J. Pelt et al. “Time delay controversy on QSO 0957+561 not yet decided”. In: 286 (June 1994). eprint: astro-ph/9401013.

[26] I. Martí-Vidal et al. “Probing the jet base of the blazar PKS 1830-211 from the chromatic variability of its lensed images. Serendipitous ALMA observations of a strong gamma-ray flare”. In: 558, A123 (Oct. 2013), A123. DOI: 10.1051/0004-6361/201322131. arXiv: 1309.0638.